On the role of spatially inhomogeneous diabatic effects upon the evolution of Mars' annular polar vortex

Masoud Rostami[a, b], Vladimir Zeitlin[a 1] and Luca Montabone[c]

[a]*Laboratoire de Météorologie Dynamique (LMD)/IPSL, Sorbonne Universités (Université Pierre et Marie Curie, UPMC) and Ecole Normale Supérieure(ENS), Paris, France*

[b] *Institute for Geophysics and Meteorology (IGM), University of Cologne, Cologne, Germany*

[c] *Space Science Institute (SSI), Boulder, CO, USA*

---

[1] Corresponding author. Email: zeitlin@lmd.ens.fr Address: LMD-ENS, 24 Rue Lhomond, 75005 Paris, France

On the role of spatially inhomogeneous diabatic effects upon the evolution of Mars' annular polar vortex

Masoud Rostami[a, b], Vladimir Zeitlin[a] ** and Luca Montabone[c]

[a]*Laboratoire de Météorologie Dynamique (LMD)/IPSL, Sorbonne Universités (Université Pierre et Marie Curie, UPMC) and Ecole Normale Supérieure(ENS), Paris, France*

[b] *Institute for Geophysics and Meteorology (IGM), University of Cologne, Cologne, Germany*

[c] *Space Science Institute (SSI), Boulder, CO, USA*

ABSTRACT

The structure of Mars' annular polar vortex is not similar to that of its counterpart on Earth and is characterised by a potential vorticity (PV) low in the vicinity of the winter pole, rather than PV monotonically increasing towards the pole. A number of persistent asymmetric high-PV patches around the central low are also typical for the Martian polar vortex. The simplest vertically averaged model of

---

**Corresponding author. Email: zeitlin@lmd.ens.fr Address: LMD-ENS, 24 Rue Lhomond, 75005 Paris, France

the Mars atmosphere (a rotating shallow water model on the polar tangent plane) with inclusion of diabatic effects is used to get clues for understanding this surprising behaviour. The standard parameterisation of radiative relaxation is applied, together with a simple parameterisation of latent heat release due to spatially inhomogeneous CO_2 deposition. The parametrisation of inhomogeneous deposition is new in this type of models, and includes dependence on the concentration of condensation nuclei, which are considered as a passive tracer. Linear stability analysis of the zonally and time averaged Mars' winter polar vortex is performed, and thus identified unstable modes are used for initialisation of high-resolution numerical simulations of their nonlinear evolution in four different configurations (adiabatic, diabatic with only radiative relaxation, only deposition, and both radiative relaxation and deposition), in order to identify the role of each process. It is shown that the combined effect of radiative relaxation and inhomogeneous deposition can account for the observed, formally unstable structure of the polar vortex, including the patches of high potential vorticity.

Keywords: Mars' polar vortex ; Barotropic Instability ; Rotating Shallow Water Model ; Radiative relaxation ; CO_2 deposition

1 Introduction

A surprising property of the Martian atmosphere is the latitudinal distribution of zonally averaged potential vorticity (PV), which has a minimum PV at the North winter pole surrounded by a circumpolar annulus of higher PV. The South pole exhibits similar characteristics of smaller intensity (Mitchell et al., 2015). Such configuration is unstable in the absence of external forcing, and is expected to evolve towards monotonous PV distribution, like e.g. the North polar vortex on Earth. Yet, this does not happen and the annular PV distribution is persistent on Mars. It should be stressed that the Martian polar vortex is annular only on average, as reanalysis datasets (Greybush et al., 2012; Montabone et al., 2014) reveal the existence of patches of high PV (Mitchell et al., 2015; Waugh et al., 2016), with time-scale of the order of a sol (a Martian mean solar day) between about 20 and 50 km altitude around the northern hemisphere (NH) winter solstice ($L_\mathrm{S} = 270°$. L_S is the solar longitude, the angular position of Mars in its orbit with respect to the position at NH spring equinox). Figure 1 shows the evolution of Ertel potential vorticity (EPV) patches during half a sol just before NH winter solstice of Martian year (MY) 24, from the Mars Analysis Correction Data Assimilation (MACDA) v1.0 reanalysis (Montabone et al., 2014). The coherence of such patches throughout local times, and their displacement with the mean flow, are remarkable in this case. Furthermore, maps of 30 *sol* mean PV show a quasi-continuous belt of high PV with an elliptical shape rather than a circular one (Mitchell et al., 2015; Waugh et al., 2016), likely forced by a stationary wavenumber-2 wave aligned with the hemisphere-scale topography, as shown by Barnes et al. (1996); Hollingsworth

and Barnes (1996). It should be noted that there are no satellite measurements of winds in the Martian atmosphere so far, and reanalysis datasets have been obtained with the support of Martian general circulation models (MGCM) (see Lewis (2003) for a general review of Mars GCMs).

It is natural to look for an explanation of the existence and longevity of the Mars' annular polar vortex in terms of diabatic effects, and indeed such attempts exist in the literature (Waugh et al., 2016; Seviour et al., 2017; Toigo et al., 2017). For example, Toigo et al. (2017) showed that the latent heat released by CO_2 "condensation" in a MGCM model tends to produce an annular polar vortex. Yet the complexity of general circulation models, including a plethora of various physical phenomena and their parameterisations, makes it difficult to isolate the particular dynamical role played by each of them. This is why simplified shallow-water models are often used for this purpose. Thus, recently Seviour et al. (2017) obtained an annular PV structure in a shallow-water model by adding thermal relaxation towards an equilibrium state. In all aforementioned studies the CO_2 deposition process is considered homogeneous, without incorporating the effects of aerosols, which may serve as "condensation" nuclei, and thus affect the spatial pattern of deposition (Although the term "condensation" is frequently used in the literature, we use the formally correct "deposition" term to avoid confusion with gas - liquid phase transition).

In this work, we use the simplest column-averaged model of the Martian atmosphere in order to understand the role of two major diabatic effects in the winter season: the radiative relaxation, and the spatially inhomogeneous CO_2 deposition

5

through the vapour-solid phase transition. The model is the rotating shallow water (RSW) model, which is not introduced in an *ad hoc* manner, but is obtained by vertical averaging of the primitive equations in pressure coordinates (Zeitlin, 2007). By the same procedure, the model allows to incorporate the profile of Mars' polar vortex as obtained from the MACDA v1.0 dataset. Using the zonally averaged profile of the polar vortex from the reanalysis, we are able to study its stability and identify the unstable modes that shape the vortex at the nonlinear stage of evolution. A major new feature and improvement of the model is that, while radiative relaxation is incorporated in the standard way, we use recipes similar to those applied for the construction of so-called moist-convective RSW models (Bouchut et al., 2009) in order to include convective fluxes produced by the latent heat release due to CO_2 deposition. Moreover, we extend this approach to allow for spatially inhomogeneous deposition with aerosols serving as deposition nuclei, as it is known that homogeneous ice nucleation is negligible in Mars' atmosphere (Wood, 1999; Colaprete and Toon, 2003; Määttänen et al., 2005). Aerosol nuclei could be any particles, such as mineral dust, water ice crystals, or micrometeorites, which have potential for triggering CO_2 ice nucleation. They are considered to be advected by the flow. We identify the dynamical role of both radiative cooling/heating and CO_2 ice deposition, and show that, even in this simple model, their combined influence allows to explain how the evolution of the most unstable mode of the zonally and time-averaged profile of Mars' polar vortex produces a structure similar to that observed in MACDA, including high PV patches and elliptic shape.

We should stress that in the present study, unlike what is frequently done with

GCMs, we do not seek to reproduce the formation of the polar vortex *ex nihilo* -a process in which the diabatic effects are surely already important. On the contrary, once the vortex is formed, we show how the adiabatic evolution towards the monotonous axisymmetric distribution is modified by each of the two diabatic effects mentioned above, and how their combination produces the characteristics observed in the reanalyses.

The paper is organised as follows. In section 2 we describe the model and introduce the new parametrisation of CO_2 deposition. We present in section 3 the background state and sketch the results of its linear stability analysis. We also present the unstable modes, which are used later for initialisation of numerical simulations of nonlinear evolution. Section 4 contains comparison of numerical simulations of the evolution of the most unstable mode of the zonally averaged polar vortex profile with and without diabatic effects, analysis of the results, and comparisons with MACDA results. Section 5 is devoted to discussion and conclusions.

2 The model

2.1 *Rotating shallow water on the polar tangent plane*

We write down the RSW equations that are obtained by vertical averaging of the adiabatic atmospheric primitive equations, with pseudo-height (Hoskins and Bretherton, 1972) as vertical coordinate, between a pair of material surfaces in the absence of forcing and dissipation. Anticipating application to a zonally averaged
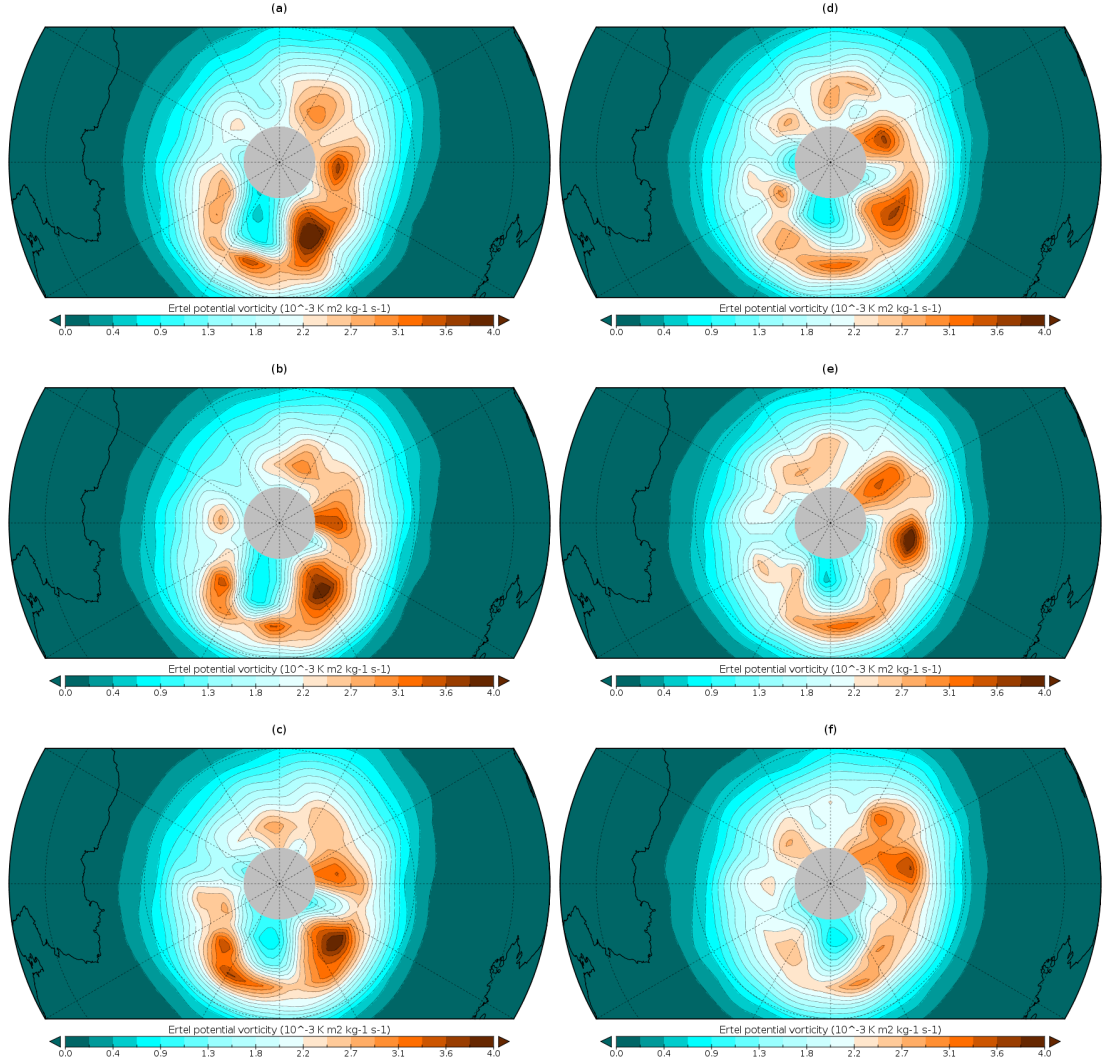
Figure 1. This figure shows the evolution of the Ertel potential vorticity on the $275K$ isentropic level (about $25km$ altitude in the NW winter polar region) from the MACDA v1.0 dataset (Montabone et al., 2014) in MY 24 at $L_S \approx 268°$ (sol-of-year=512). Each panel is separated by two hours, for a total evolution time of half a sol. The order of the sequence is from panel (a) to (f), with panel (a) corresponding to 02:00 a.m. at $0°$ longitude. The longitude-latitude grid (dotted lines) is $30° \times 30°$. The projection is orthographic, centred on the North pole. The prime meridian is pointing downward. The grey area around the North pole is where the calculation of the latitudinal derivative of the zonal wind is not carried out (we use a conservative approach to avoid possible artifacts in the calculation of EPV from MACDA v1.0 dataset at very high latitudes). Note that we use $c_p = 820 \ JKg^{-1}K^{-1}$ to define the isentropic levels, consistently with the study by Mitchell et al. (2015). If one uses $c_p = 745 \ JKg^{-1}K^{-1}$ as in other studies, these figures correspond to an isentropic level of 287 K.

8

polar vortex, we rewrite the equations in cylindrical coordinates. We will not work on the whole rotating sphere, but rather limit ourselves to the polar region, which will be considered in the so-called gamma-plane approximation, i.e. the tangent plane approximation with the curvature correction to the Coriolis parameter.

$$\frac{D\boldsymbol{v}}{Dt} + (f + \frac{\boldsymbol{v}}{r})(\hat{\boldsymbol{z}} \times \boldsymbol{v}) = -g'\boldsymbol{\nabla}_H h, \tag{2.1a}$$

$$\frac{Dh}{Dt} + h\boldsymbol{\nabla}_H.\boldsymbol{v} = 0. \tag{2.1b}$$

Equation (2.1a) expresses momentum conservation in the fluid layer in the presence of the Coriolis force, and equation (2.1b) expresses conservation of mass. In these equations (r, θ) are polar coordinates in the tangent plane, $\hat{\boldsymbol{z}}$ is the unit vector normal to the plane, $\boldsymbol{v} = u\hat{r} + v\hat{\theta}$, u and v are radial and azimuthal components of the horizontal velocity $\boldsymbol{v}$, respectively. $g' = g(\theta/\theta_0)$ is effective gravity defined by the mean potential temperature of the atmospheric layer θ normalised by a reference value θ_0, and f is the Coriolis parameter, h is the thickness of the layer defined as pseudo-height (note that the atmospheric shallow water model is "upside-down", in a sense that the free surface is on the ground and the fixed pseudo-height (pressure) level is on the top, while geopotential is constant on the ground, cf. (Bouchut et al., 2009; Rostami and Zeitlin, 2018), $D/Dt = \partial_t + \vec{\boldsymbol{v}}.\boldsymbol{\nabla}_H$ is the material derivative, and $\boldsymbol{\nabla}_H = \hat{r}\partial_r + \hat{\theta}(1/r)\partial_\theta$ is the two-dimensional gradient in cylindrical coordinates. The Coriolis parameter in the gamma-plane approximation has the form $f = f_0 - \gamma r^2$, where $f_0 = 2\Omega$, and Ω is the angular velocity of the planet's rotation. In fact, at latitude ϕ the Coriolis parameter is $f = 2\Omega \sin \phi$, and

9

the gamma-plane formula retains only the first non-trivial term in the Taylor expansion of $\sin\phi$ at $\phi = \pi/2$. The gamma-plane approximation can be "improved" by including subsequent terms of the Taylor expansion. We will be using sponges at the boundaries of the calculational domain in numerical simulations below, which, roughly, correspond to radiative boundary conditions allowing to dump inertia-gravity waves produced by the evolution of the vortex. Although topography can be straightforwardly introduced in the model, we will not include it in the present study.

2.2 Inclusion of diabatic effects

2.2.1 Radiative relaxation

The first diabatic effect to be included in equations (2.1a) - (2.1b) is the radiative relaxation of pressure field towards an equilibrium configuration of thickness in pseudo-height coordinates $h = H(r, \theta)$, with some relaxation time τ_r. Thus, to include this effect, the equation (2.1b) is modified following the well-known equation (common for all atmospheres):

$$\frac{Dh}{Dt} + h\boldsymbol{\nabla}_H.\boldsymbol{v} = -\frac{h - H}{\tau_r}. \tag{2.2}$$

This parametrisation has been applied to Mars' polar vortex in Seviour et al. (2017), and is also used for Earth's polar vortex, e.g. Rong and Waugh (2004), where a relaxation toward a monotonic equilibrium profile has been considered. It is known that the radiative relaxation rate on Mars is much faster than that on Earth (Goody and Belton, 1967; Imamura and Ogawa, 1995; Eckermann et al.,

2011). Seviour et al. (2017) tested weak and strong relaxation with $\tau_r = 10, 2, 0.5$ *sols*. The simplest parameterisation is that with radiative heating and cooling rates having the same scale for all altitudes. Yet, parametrisations of radiative heating and cooling rates in MGCMs suggest departures from the local thermodynamic equilibrium above ≈ 80 km altitude (López-Puertas and López-Valverde, 1995; López-Valverde et al., 1998; González-Galindo et al., 2009), although we will neglect them.

2.2.2 CO_2 deposition

The second diabatic effect is specific for Mars and consists of the latent heat release due to deposition of CO_2, which is the main component of the Martian atmosphere (about 96% based on the latest measurements by Curiosity rover (Mahaffy et al., 2013)), and formation of CO_2 ice clouds. Martian CO_2 ice clouds have been observed mostly during the polar nights in the lower troposphere (Pettengill and Ford, 2000; Hayne et al., 2012; Hu et al., 2012), but also in the equatorial and mid-latitude mesosphere (González-Galindo et al., 2011). The primary mechanism of CO_2 ice-cloud formation in the Martian atmosphere is heterogeneous nucleation on the dust particles (Määttänen et al., 2005; Listowski et al., 2014). It is worth noting that by dust in this article we mean any type of deposition nuclei, which can be of different origins: mineral dust elevated from the ground by winds, water ice crystals, or any type of micrometeorites. A sufficient local concentration of nuclei is assumed to be a necessary condition for CO_2 deposition in this study. Deposition in Mars GCM models has not been coupled to aerosols so far, and only depends on the temperature, while here the inhomogeneity introduced by the

aerosol spatial distribution will play a decisive role in both CO_2 deposition and radiative relaxation.

In the simplest version of the model we are using (2.1a) - (2.1b), the potential temperature θ is considered to be horizontally uniform. So the deposition phase transition in the model is controlled uniquely by the remaining thermodynamical variable, the pressure h, and starts once the pressure is higher than some threshold pressure, h_{th}. The deposition then leads to pressure relaxation towards the threshold value with a characteristic time τ_c. The deposition threshold pressure is taken to be above the equilibrium pressure H, by a tunable amount ϵ^*. A necessary condition to trigger the deposition is that the bulk amount of nuclei in the air column, N, also exceeds some threshold value, N_{th}. The deposition of CO_2 is accompanied by a latent heat release, which creates a vertical convective flux resulting in a sink in the mass conservation equation. Additional convective fluxes are easily introduced in the derivation of RSW model by vertical averaging the primitive equations, as was shown for the moist-convective RSW in Bouchut et al. (2009). We follow here the recipe of this paper, although the origin of the convective flux is different. Like in the moist-convective RSW, the momentum equation is unchanged, while the mass conservation acquires sources/sinks due to radiative relaxation and CO_2 deposition, and takes the following form:

$$\frac{Dh}{Dt} + h\boldsymbol{\nabla}_H.\boldsymbol{v} = -\frac{h - H}{\tau_r} - C. \tag{2.3}$$

According to what was just said, the mass flux due to deposition is

$$C = \alpha^* \frac{h - h_{th}}{\tau_c} \mathcal{H}(h - h_{th})(N - N_{th})\mathcal{H}(N - N_{th}), \qquad (2.4)$$

where $\mathcal{H}$ denotes Heaviside (step-) function, the constant α^* can be absorbed in the relaxation time τ_c without loss of generality, and the deposition threshold is restricted by a threshold pressure given by

$$h_{th} = H(r) + \epsilon^*. \qquad (2.5)$$

As follows from (2.4), we consider that deposition can not take place if the bulk amount of nuclei in the air column N is below N_{th}, and stops once N drops below this threshold. The nuclei conservation equation is given by

$$\frac{DN}{Dt} + N\boldsymbol{\nabla}_H.\boldsymbol{v} = -\delta C + S, \qquad (2.6)$$

where the first term in the r.h.s. corresponds to depletion of nuclei due to deposition, and the second one is a nuclei source. We will not dwell into discussion of parameterisations of S (for example, the one proportional to the wind $\boldsymbol{v}$ could be used, like what is used for surface evaporation, see e.g. Rostami and Zeitlin (2017)), and will consider for simplicity that production and depletion of nuclei are either negligible, or compensate each other, i.e. that the r.h.s. of (2.6) is zero, and deposition nuclei (i.e the tracer field) are just transported, but not produced, nor eliminated.

The values of parameters, τ_r, τ_c, N_{th}, ϵ^* used in numerical simulations presented in this paper are given in Table 1. For simplicity N is initialised with a uniform value close to N_{th}. Deposition time scale τ_c, which is the key parameter, is chosen

Table 1

Initial conditions and parametrisations of the numerical experiments. Adiabatic: diabatic effects switched off, R: environment including just the radiative relaxation, D: environment including only the CO_2 deposition, RD: environment including both radiative relaxation and deposition, N_{th}: threshold value of bulk concentration of nuclei above which deposition occurs. Δt: the numerical time step. Fixed parameters of all simulations: $\epsilon = 0.2489, \alpha = 4.1, \beta = 2.3, m = 3.2, L_d = 1740\ km, r_0 = 0.35, r_{00} = 0.4$.

Parameter	Adiabatic	R	D	RD
τ_r	-	$0.5\ sol$	$\infty\ sol$	$0.5\ sol$
τ_c/α^*	-	-	$5\Delta t$	$5\Delta t$
ϵ^*	-	-	0.001	0.001
N_{th}	-	-	0.9	0.9

to be fast: just few numerical time steps. As in simulations with moist-convective RSW (Bouchut et al., 2009), this poses no numerical problems. Lower values of τ_c result in stronger deposition. The results of linear stability analysis depend on L_d, see below.

In what follows we will first use the adiabatic version of the model (2.1a), (2.1b) in order to identify the unstable modes of the zonally and time-averaged Mars' polar vortex, and then use these latter to initialise numerical simulations of the nonlinear evolution of instabilities in adiabatic and diabatic versions of the model. We will diagnose nonlinear evolution of the instabilities with the help of potential vorticity (PV). Indeed, as is well-known, the adiabatic version of the model (2.1a),

(2.1b) possesses a Lagrangian invariant, the potential vorticity $q = (\zeta + f)/h$:

$$\frac{D}{Dt}\left(\frac{\zeta + f}{h}\right) = 0, \tag{2.7}$$

where ζ is the relative vorticity in the tangent plane: $\zeta = \hat{\boldsymbol{z}} \cdot \boldsymbol{\nabla} \times \boldsymbol{v}$. In the presence of diabatic effects PV acquires sources/sinks

$$\frac{D}{Dt}\left(\frac{\zeta + f}{h}\right) = \left(\frac{\zeta + f}{h^2}\right)\left(\frac{h - H}{\tau_r} + C\right). \tag{2.8}$$

which modify its evolution.

3   Background vortex and its instabilities

3.1   A reminder on vortex solutions and linear stability analysis

The first stage of our analysis is identification of unstable modes of the zonally and time-averaged Mars' polar vortex. Azimuthally-symmetric stationary state with a given velocity profile $V(r)$, which we retrieve from MACDA data below, is a solution of the equations (2.1a), (2.1b) provided $V(r)$ and the pressure (thickness) $H(r)$ are in cyclo-geostrophic (or gradient wind) equilibrium:

$$(\frac{V}{r} + f)V = g\partial_r H. \tag{3.1}$$

Linear stability of any solution of this kind is analysed by the standard means. The equations (2.1a), (2.1b) are linearised, considering small perturbations of the axisymmetric background flow, denoted by primes. It is convenient to work with non-dimensional equations, and we will be using the following scaling, with non-

dimensional variables marked with an asterisk:

$$(u', v', V)(r, \theta, t) = L_d f_0 (u^*, v^*, V^*)(r^*, \theta^*, t^*), \tag{3.2a}$$

$$r = L_d r^*, \theta = \theta^*, t = \frac{1}{f_0} t^*, \quad H(r) = H_0 H^*(r^*), h' = H_0 \eta^*. \tag{3.2b}$$

Here H_0 is a characteristic thickness, and L_d is the Rossby deformation radius $L_d = \sqrt{gH_0}/f_0$. The advantage of this non-dimensionalisation is that it is based on a single adjustable parameter, L_d, while f_0 is fixed for a given planet.

We are looking for the normal-mode solutions with harmonic dependence on time and polar angle

$$(u^*, v^*, \eta^*)(r^*, \theta^*, t^*) = Re[(i\tilde{u}, \tilde{v}, \tilde{\eta})(r^*)e^{i(l\theta^* - \omega t^*)}], \tag{3.3}$$

where l and ω are the azimuthal wavenumber and the frequency, respectively. The corresponding eigenproblem can be written as:

$$\begin{bmatrix} \dfrac{lV^*}{r^*} & \left[\sin(\phi) + \dfrac{2V^*}{r^*}\right] & -D_{r^*} \\[3mm] \left[\sin(\phi) + \dfrac{V^*}{r^*} + D_{r^*}V^*\right] & \dfrac{lV^*}{r^*} & \dfrac{l}{r^*} \\[3mm] H^*D_{r^*} + \dfrac{1}{r^*}D_{r^*}(r^*H^*) & \dfrac{lH^*}{r^*} & \dfrac{lV^*}{r^*} \end{bmatrix} \times \begin{bmatrix} \tilde{u} \\[3mm] \tilde{v} \\[3mm] \tilde{\eta} \end{bmatrix} = \omega \begin{bmatrix} \tilde{u} \\[3mm] \tilde{v} \\[3mm] \tilde{\eta} \end{bmatrix}, \tag{3.4}$$

with D_{r^*} denoting differentiation with respect to r^*. Complex eigen-frequencies $\omega = \omega_r + i\omega_I$ with positive imaginary part ($\omega_I > 0$), correspond to instabilities with linear growth rate $\sigma = \omega_I$. In the formulas above $\sin\phi$ in the Coriolis parameter should be understood in the sense of Taylor expansion in r, where the first two

terms correspond to the gamma-plane approximation, but higher terms could be also retained, heuristically.

Numerical analysis of the eigenproblem (3.4) is performed by the pseudospectral collocation method (Trefethen, 2000). The system is discretised over an N-point grid in the radial direction, and D_{r^*} becomes the Chebyshev differentiation operator. To avoid the Runge phenomenon, Chebyshev collocation points are used, with a stretching in the radial direction allowing to accumulate the collocation points in the most dynamically interesting region near the centre of the vortex. The eigenproblem (3.4) is singular, possessing so-called critical levels, where the angular velocity of the eigenmodes ω/l is equal to the local angular velocity of the flow V^*/r^*. Numerical solutions of (3.4) can produce pseudo-modes which are not smooth at critical levels, and not converge to smooth solutions with increasing resolution. Such modes were carefully analysed and eliminated. We should say that stability analyses of atmospheric jets are known in literature for a long time, e.g. Hartmann (1983), including jets on Mars (Michelangeli et al., 1987). However, they are usually done 1) with *ad hoc* analytic velocity profiles, and 2)within the quasi-geostrophic model which, in our case, is a small Rossby number limit of the system (2.1a), (2.1b), with the velocity field given in terms of the geostrophic stream-function, and thus having only very weak divergence. We perform the stability analysis of the velocity profile fitted from the data, and find the unstable modes, which we use later for initialisations of numerical simulations in the "full" model, as even a small divergence is crucial in determining the transport properties of the flow.

17

3.2   Stationary barotropic Mars' polar vortex and its instabilities

To construct a stationary solution of our shallow water model corresponding to the Martian winter polar vortex we use the MACDA v1.0 dataset (Montabone et al., 2014). As we are mostly interested in the atmospheric configuration that occurs during middle winter, when deposition and related latent heat release are expected (Hu et al., 2012), we consider data about the NH winter solstice ($L_\mathrm{S} \approx 270°$) of MY 24. We take 14 layers up from the surface in the MACDA dataset, which corresponds to the pressure range $0.9995 P_s - 0.2 P_s$, where P_s is the surface pressure. Thus $H_0 \approx 16.5 km$, and $L_d \approx 1750 km$. The background velocity profile is obtained by vertical, zonal, and solar longitude (i.e. time) averaging within $270° \leq L_\mathrm{S} \leq 271°$ of corresponding MACDA data. The corresponding pseudo-height profile follows from the cyclo-geostrophic balance (3.1). We thus obtain a full stationary solution of the equations of the model whose linear stability can be analysed by the above-described method. The results both on linear stability and on nonlinear saturation of the instability are sensitive to the value of the Rossby deformation radius L_d.

Instead of numerical interpolation of the velocity profile data obtained by the above-described procedure, it is convenient to use its analytic fit, which can be achieved by a simple parametrisation with a small number of parameters. The fit

18

for azimuthal velocity of the stationary vortex we are using is as follows:

$$V(r) = \begin{cases} \epsilon \dfrac{\left[(r-r_0)^{\alpha} e^{-m(r-r_0)^{\beta}}\right]}{max\left[(r-r_0)^{\alpha} e^{-m(r-r_0)^{\beta}}\right]}, & r \geq r_{00}. \\[2em] m_0 r, & r < r_{00} \end{cases} \tag{3.5}$$

In this formula r is the non-dimensional distance from the vortex center, ϵ measures the intensity of the velocity field in the circumpolar jet, r_0 gives the non-dimensional radius of maximum wind (RMW), and other parameters allow to fit the shape of the distribution. As the center of the Martian winter polar vortex is relatively calm, with low-speed winds, we suppose a slow solid rotation in this region, i.e. linear $V(r)$ with a gentle slope $m_0 \approx 0.02\epsilon$. The parameter r_{00} gives the size of this domain. A cubic Hermite interpolation between the two regions is done to prevent jump appearance in vorticity profile. An advantage of this parametrisation is the possibility to tune the ascending or descending trend of the wind near and far from the peak. The velocity profile is normalised by its maximum, so the maximum value of velocity is equal to ϵ. We list in Table 1 the values of the parameters we have chosen, together with parameters of diabatic corrections which are used in nonlinear simulations below. The upper left panel of Figure 2 provides a comparison of the MACDA data with the fit (3.5) using the values of parameters given in Table 1.
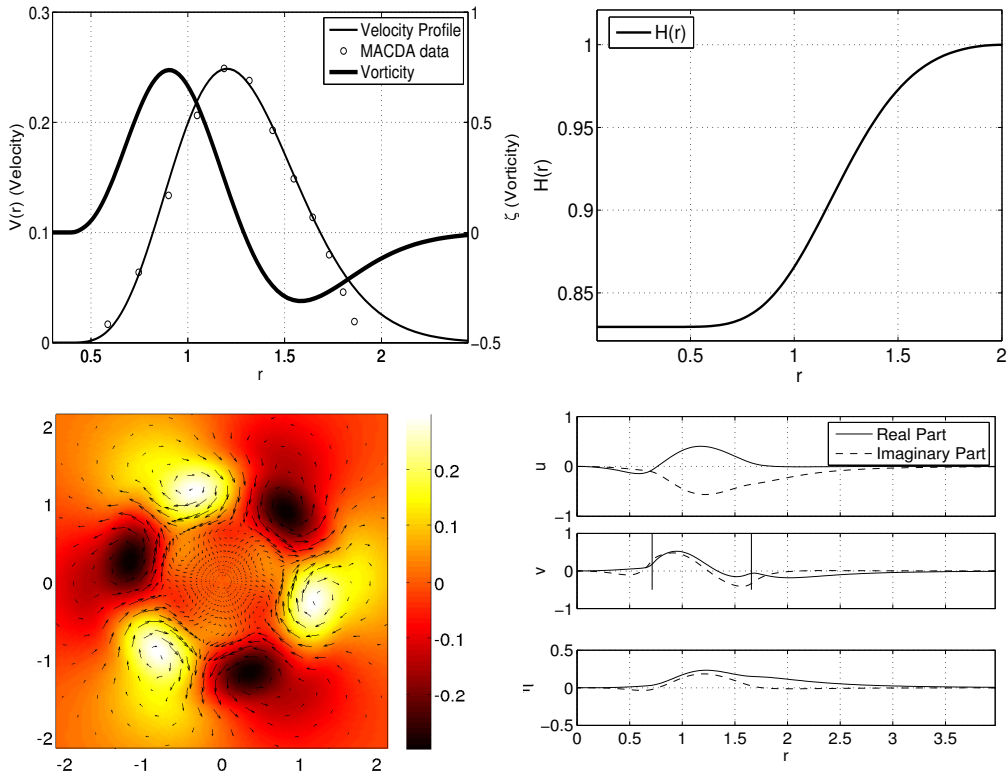
Figure 2. Upper left panel: radial profile of barotropic azimuthal velocity of Mars'
north polar vortex superimposed on vertically and time-averaged MACDA data, and
the corresponding profile of relative vorticity. Upper right panel: thickness $H(r)$ of the
background vortex. Lower left panel: $2D$ structure of the most unstable mode with $l = 3$.
Colours: pressure (thickness) anomaly, arrows: velocity field. Lower right panel: radial
structure of the most unstable mode. Vertical lines indicate the critical levels.

3.3   Results of the linear stability analysis of the zonally averaged vortex profile

We omit the details of computations following the procedure sketched in Section
3, and present only the main results and their analysis. For the barotropic velocity
profile $V(r)$, described in subsection 3.2, the most unstable modes have azimuthal
wavenumbers $l = 2$ and $l = 3$, with a slightly higher growth rate for the latter.

20
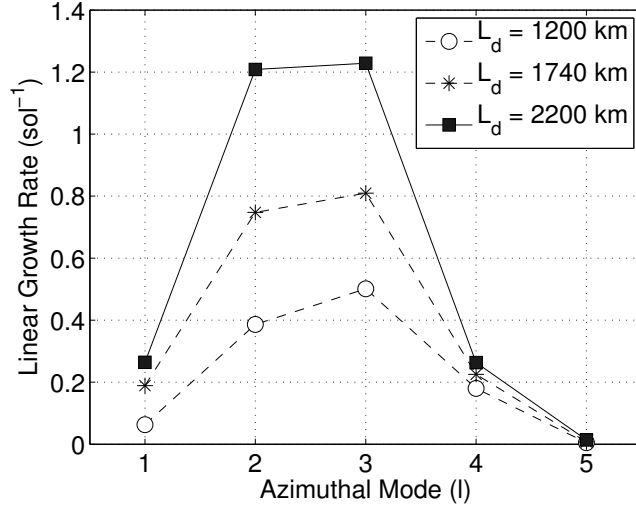
Figure 3. Linear growth rate of the barotropic structure as a function of azimuthal wavenumber at different values of the Rossby deformation radius. $L_d \approx 1200, 1740, 2200 km$ correspond to vertical averaging over $12, 14, 16$ layers, respectively.

The azimuthal and radial structure of the unstable mode with $l = 3$ is presented in Figure 2, together with the background vortex profile. Nevertheless, the growth rates of modes with azimuthal wave-numbers $l = 1, 4$ are not negligible. This result is compatible with those of Barnes et al. (1993) at $L_d \approx 1700 - 1800 km$. Figure 3 represents a variation of the linear growth rate with azimuthal wavenumber for different values of L_d. Linear stability analysis of the profile (3.5) demonstrates that when the RMW of the background velocity profile is closer to the North Pole with higher curvature at the RMW, the most unstable mode shifts to lower azimuthal wavenumbers and higher growth rates, and vice versa. On this basis we can expect strong wavenumber two and wavenumber three instabilities with growth rates larger than $1 \ sol^{-1}$ in the Martian upper atmosphere during winter, as velocity peak is higher and closer to the pole in the upper layers. This is com-

patible with findings of Conrath (1981), where a stationary wavenumber 2 pattern in the upper atmosphere was revealed by using Mariner 9 Infrared Interferometer Spectrometer (IRIS) data. The gradient of PV in MACDA data in the lower layers is much smaller than its counterpart in the upper layers, and the RMW is larger than in the upper ones. So if the upper layers are excluded from vertical averaging, the growth rates of corresponding unstable modes become smaller and the most unstable azimuthal wavenumber shifts to higher values, and vice versa. Increasing the amplitude of the initial velocity, i.e. the Rossby number, leads to an increase of growth rates, but the azimuthal wavenumber of the most unstable mode remains the same. This relationship is almost linear, similarly to what was found in (Rostami and Zeitlin, 2017; Rostami et al., 2017). Although we did not introduce them, adding Ekman friction and viscosity would lead to lower values of phase speeds and growth rates, cf. (Barnes, 1984).

4 Nonlinear evolution of instability

Once the unstable modes of the stationary polar vortex are identified, the question arises about nonlinear evolution of the instability. In the present section we compare the adiabatic evolution of the instability with diabatic evolution in the configurations including 1) only classical radiative relaxation (R), with deposition term switched off in (2.3), but including the passive tracer N, 2) only spatially inhomogeneous CO_2 deposition (D), due to the coupling of the pressure field with the tracer, with deposition term switched on but radiative relaxation term switched off in (2.3), and 3) both radiative relaxation and CO_2 deposition (RD). We per-

form fully nonlinear numerical simulations using a finite-volume scheme designed for moist-convective RSW (Bouchut et al., 2009). Inclusion of the radiative relaxation in the scheme is straightforward, and the deposition corrections discussed in section 2 are incorporated along the same lines as condensation in the moist-convective RSW. In order to analyse the development of the barotropic instability, the variables u, v, h are initialised by superimposing a small perturbation corresponding to the most unstable mode with $l = 3$ onto the background vortex profile obtained by vertical averaging from MACDA data. The initial distribution of N, which is N_0, is uniform (0.005 below N_{th}). It should be noted that changes in the scale of N and N_{th} can be absorbed by rescaling of the relaxation time, and it is the relative difference between the two which is the most important factor: the smaller the difference the stronger the effect.

Comparisons of adiabatic and diabatic (in different configurations) nonlinear evolution of the unstable mode as seen in the PV field are presented in Figure 4. In all environments, the growing initial $l = 3$ perturbation leads to formation of the triangular eye-wall at early stages, which is gradually transformed into a quasi-annular belt of higher PV around the eye. Yet, re-distribution of PV in the belt, leading to spatial non-uniformity, occurs rather early ($t \approx 150 f^{-1}$) in the simulations involving deposition (the second and the fourth rows of Fig. 4), while this is not the case in the adiabatic simulation nor in the one with radiative relaxation only. Due to space limitations we skip the snapshots between $t = 200 f_0^{-1}$ and $t = 300 f_0^{-1}$ in all simulations. They show an evolution towards the last displayed state without qualitative disruptions. The annular PV structure is clearly visible in all cases at initial steps. As time goes on the form of the PV belt is modu-

23

lated by other azimuthal modes emerging due to nonlinear interactions in course of evolution. We show behavior of the normalised amplitudes of azimuthal modes of the perturbation, extracted from the simulations of nonlinear evolution of the instability in Figure 5. As follows from the Figure, the $l = 1$ and $l = 2$ modes are growing faster than modes with $l = 4$ and $l = 5$ during instability saturation. However, with the choice of parameters made, the evolution in configurations with deposition has a tendency to saturate the $l = 2$ mode, which is mainly responsible for the ellipticity, faster then in purely radiative configuration. Differences among four configurations are manifest in Figure 4. Yet, although patches of higher PV appear in simulations with deposition at later stages (the two last columns of the Figure), they are less pronounced than in the reanalysis data. In order to track the patchiness of the PV field we continued simulation for even longer times. The results are presented in Figure 6, and clearly show that only the combination of radiative relaxation and deposition gives a PV field qualitatively similar to the reanalysis, while relaxation or deposition alone do not. The form of the PV belt in different configurations is consistent with Figure 5 and is corroborated by further evolution of the azimuthal modes presented in Figure 7.

In order to better quantify the influence of both diabatic effects upon the annularity of the resulting distributions of potential vorticity and velocity, we present radial distributions of zonally and time averaged PV and velocity at the late stages of the evolution of the instability in the left and right panels of Figure 8, respectively. As follows from all the displayed figures, the influence of diabatic effects upon the developing instability is drastic. While the adiabatic evolution follows the standard scenario of growth and breaking of the unstable mode, which leads

24

to filling up the PV minimum in the centre of the vortex and forming a monotonous PV profile, this process is arrested in the presence of radiative relaxation, which leaves the PV distribution hollow. Deposition alone, D, leads to non-uniform filling of the centre of the PV distribution, with formation of high PV patches, as compared with the adiabatic evolution. Nevertheless, in this case the ring of high PV collapses at later times and gives a centred distribution of PV, like the diabatic one. Together, radiative relaxation and deposition lead to hollow PV distribution with high PV patches in the PV belt around the PV minimum at the centre. We checked the sensitivity of the just described scenarios to the values of parameters. The results are presented in Figure 9, and show that big qualitative differences between D, R, and RD scenarios do not change with the changes of N_0, ϵ^* and τ_r, although some quantitative differences, e.g. in the height of the PV maximum, do exist. The presence of patches is clearly visible at all stages of the deposition-relaxation scenario, and is qualitatively similar to what is observed in MACDA data, cf. Figure 1. Such patches were also detected in the Ensemble Mars Atmosphere Reanalysis System (EMARS) dataset and GCM simulations, cf. (Waugh et al., 2016). In order to quantify the patchiness of each case in a robust way, we apply a spatio-temporal diagnostics of patchiness based on its definition, which is the variance of PV about the mean distribution of PV. The results are presented in Figure 10, and show that, as the time goes on, the patchiness of both D and R falls down, while RD is enhanced similarly to results from reanalyses. The presence of these zones of high PV explains the average enhancement of PV at the RMW observed in Figure 8. Yet the ellipticity of the annulus is better accounted for in the purely radiative simulation, cf. Figures 6 and 7. It should be emphasised that

the initialisation was made with solely the most unstable mode with $l = 3$, and the system keeps memory of this for long times.

In order to understand the origin of enhanced zones of PV in simulations with deposition, we trace in Figures 11 and 12 the evolution of the dust field N in all simulations. We should recall that the convective sink of any nature enhances PV, as follows from (2.8). The related change in h leads to additional radiative relaxation and the two source/sink terms in (2.3) thus influence each other. The deposition sink is strongly inhomogeneous in space as it is operational only when a high concentration of N occurs in the region of strong enough pressure. As follows from Figures 11 and 12, the zones of high N are much more intermittent and have more complex structure in the configurations with deposition, as compared to the purely radiative configuration, which explains the patchiness of enhanced PV. Let us recall that we take the initial distribution of dust as uniform in all configurations. Its evolution is well correlated with that of the divergence field. The dust is rapidly expelled out of the center of the vortex, and evolves around the RMW and beyond. Although this has no direct relation to the goal of this paper, we should emphasise that the evolution of the divergence field displays bursts of emission of inertia-gravity waves related to the convective events due to deposition (not shown here).
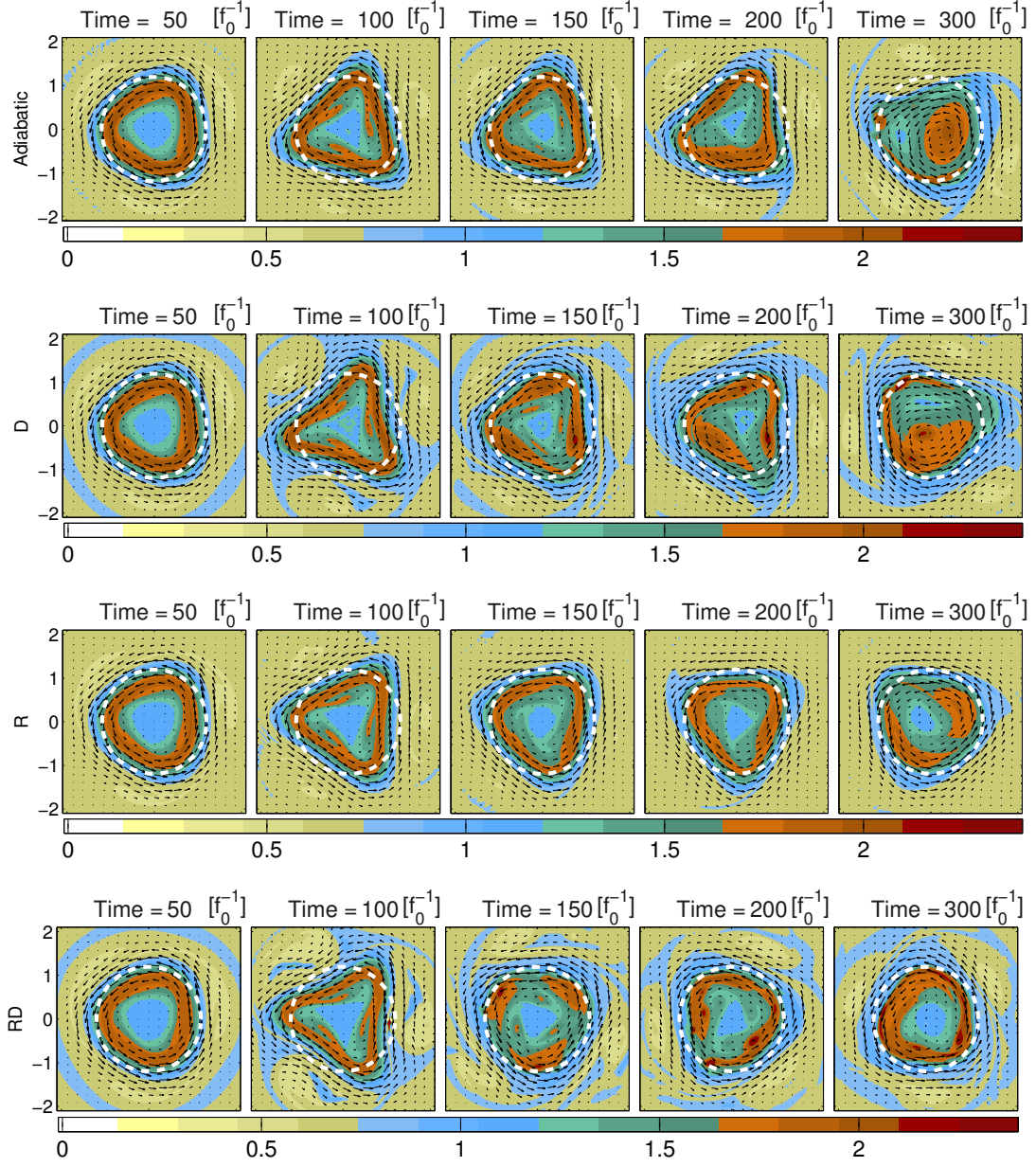
Figure 4. Nonlinear evolution of the $l = 3$ instability in different environments, as seen in PV field measured in units of H_0/f_0. From top to bottom: adiabatic evolution, evolution with CO_2 deposition only (D), evolution with radiative relaxation only (R), evolution with both radiative relaxation and deposition (RD). White dashed lines indicate initial radius of maximum wind (RMW). $12.5 \, [f_0^{-1}] \approx 1 [\, sol]$.
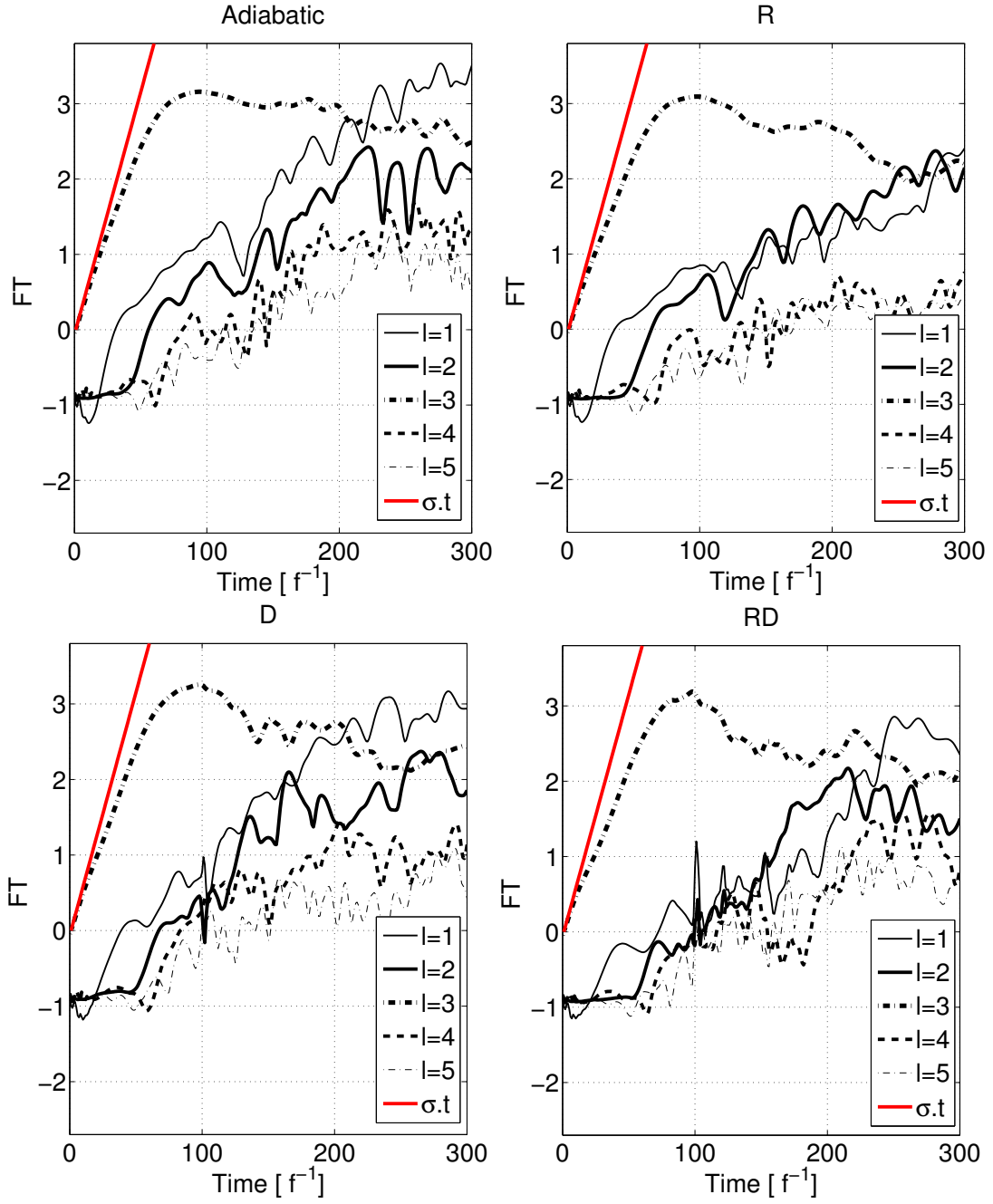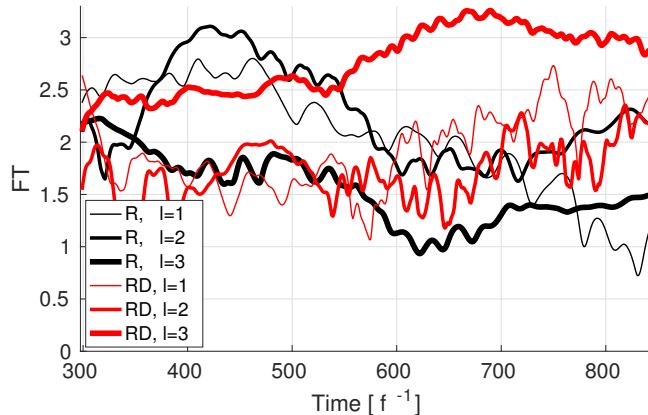
Figure 5. Evolution of the logarithm of the normalized amplitudes of the Fourier modes of the azimuthal velocity during the saturation of the $l = 3$ instability at four different configurations of Table 1.

28
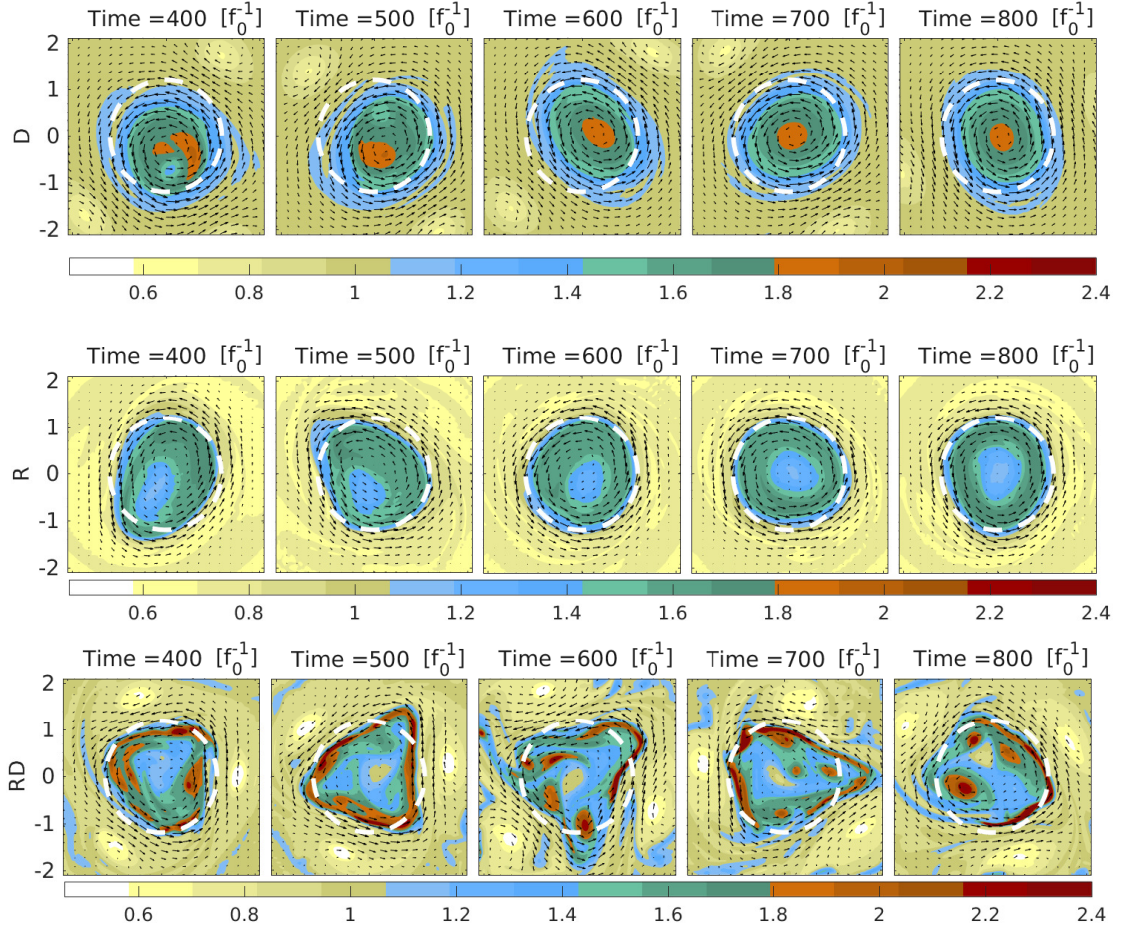
Figure 6. Late -time evolution of the PV field in D, R, and RD configurations.

5   Conclusions and discussion

We introduced a new simple parametrisation of spatially inhomogeneous CO_2 deposition and related convective fluxes into a vertically integrated model of the Martian polar atmosphere, together with a simple parametrisation of radiative relaxation. The inhomogeneous CO_2 deposition is due to the coupling with a deposition nuclei field,transported by the flow. We were able to identify dynamical

Figure 7. Evolution of the logarithm of the normalized amplitudes of the dominant Fourier modes of the azimuthal velocity at the late stages of the saturation of the $l = 3$ instability in R and RD configurations.
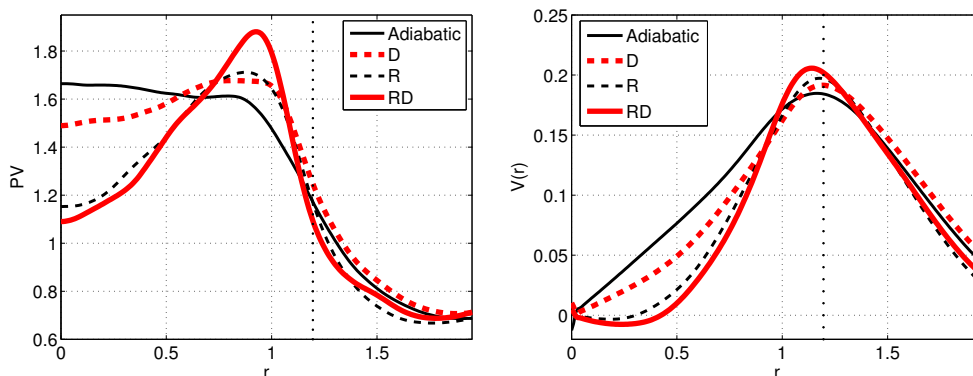
Figure 8. Radial distribution of zonal means of PV (left panel) and zonal velocity (right panel) averaged over a period of time from $[250f_0^{-1}]$ to $[300f_0^{-1}]$ in different environments (see Table 1). Vertical dotted line represents the radius of maximum wind of the non-perturbed vortex.

consequences of radiative relaxation and CO_2 deposition, and reproduce patches of high potential vorticity, which are observed in atmospheric reanalysis datasets.

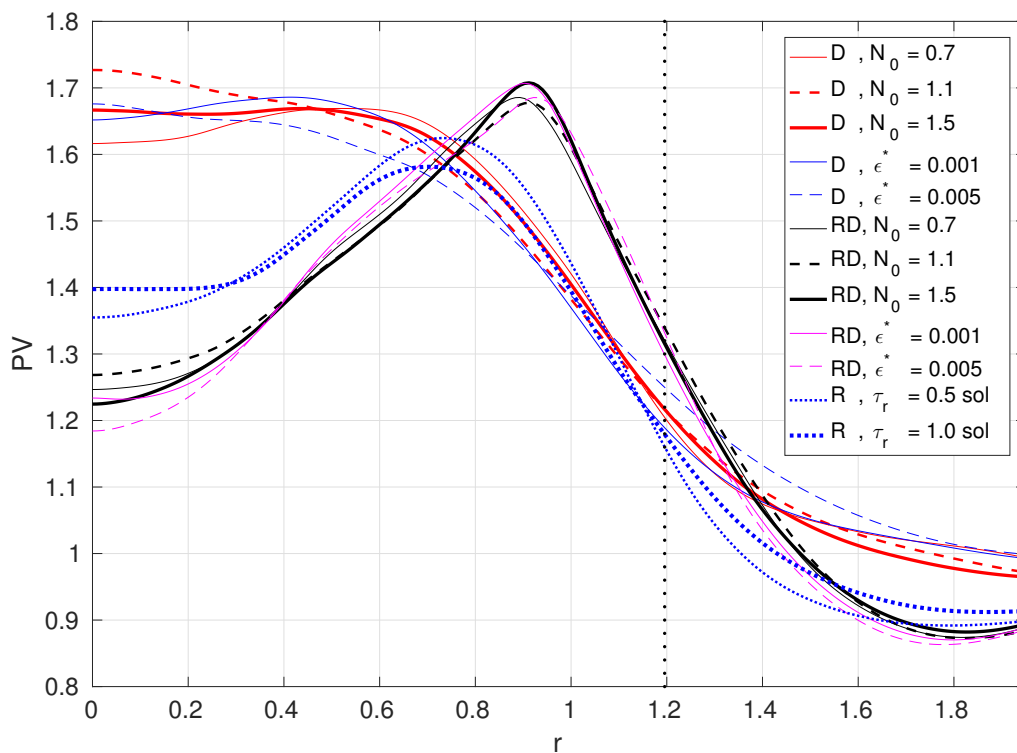We show that it is the barotropic instability of the azimuthally averaged Mars' po-

Figure 9. Sensitivity of radial distributions of zonally and time averaged PV to different values of the initial uniformly distributed concentration of dust N_0, radiative relaxation time (τ_r), and ϵ^* in different environments (see Table 1). The vertical dotted line represents the radius of maximum wind of the non-perturbed vortex. Time interval: from $[0f_0^{-1}]$ to $[900f_0^{-1}]$.

lar vortex profile that governs the evolution of the vortex, although the observed structure of the polar vortex would not survive without diabatic effects. The radiative effects are shown to play a crucial role in maintaining the PV minimum at the centre of the Martian polar vortex, provided relaxation time is short enough, which confirms the results of Seviour et al. (2017); however, the radiative effects alone are not enough to explain the patches of high PV observed in atmospheric reanalysis
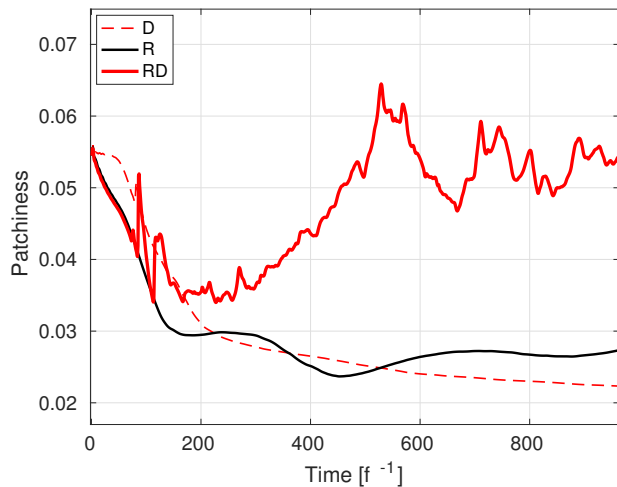
31

Figure 10. Patchiness of PV, measured as variance about the mean, in different environments (see Table 1).

datasets. At large relaxation times the hollow PV tower cannot resist the instability. At low Rossby deformation radii, the hollow PV tower is maintained even at larger relaxation times. On the other hand, combination of thermal relaxation and the inhomogeneous CO_2 deposition triggered by nucleation is shown to lead the appearance of patches of high-PV inside the annulus, similar to what is observed in MACDA and EMARS datasets. This is the key new finding of the present work demonstrating dynamical influence of the deposition which is conditioned by the presence of deposition nuclei in a sufficient amount. We should emphasize that linking radiative properties to the presence of tracers (e.g. dust) can be done in the model along the same lines as in section 2.2.2. We also showed that qualitative differences among the relaxation-deposition scenario and others are not sensitive to the particular choice of values of the parameters of deposition and relaxation, within a reasonable range.

The key advantage of the simple rotating shallow water model we are using is
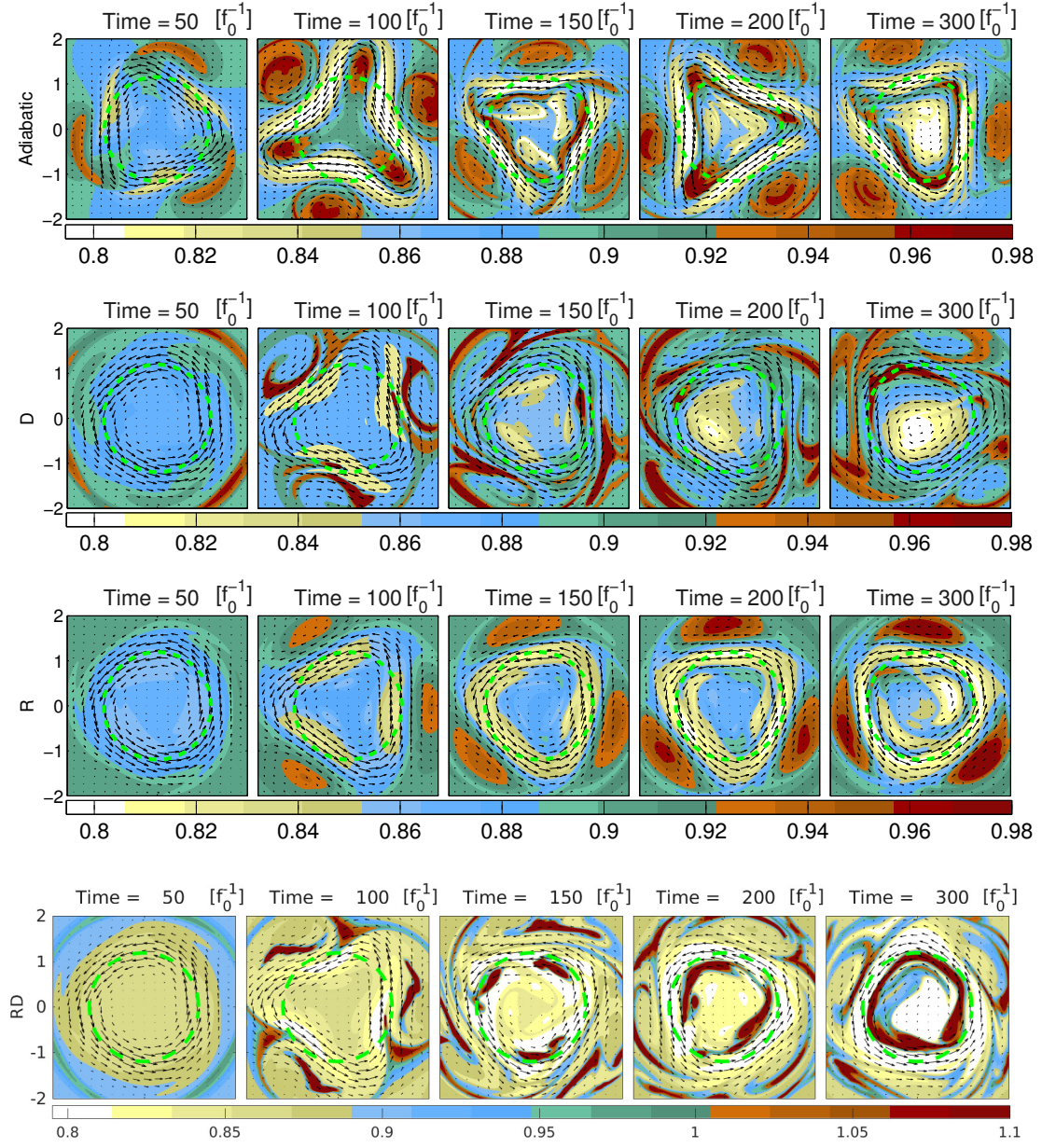
32

Figure 11. Evolution of the tracer (dust) field during nonlinear saturation of the $l = 3$ instability in different environments. From top to bottom: adiabatic evolution, evolution with deposition only (D), evolution with radiative relaxation only (R), evolution with both radiative relaxation and deposition (RD). The thick dashed lines indicate the initial radius of maximum wind (RMW). 12.5 $[f_0{}^{-1}] \approx 1[\ sol]$. Only a part of the calculational domain is presented. The colorbar in the RD case has been changed for clarity.
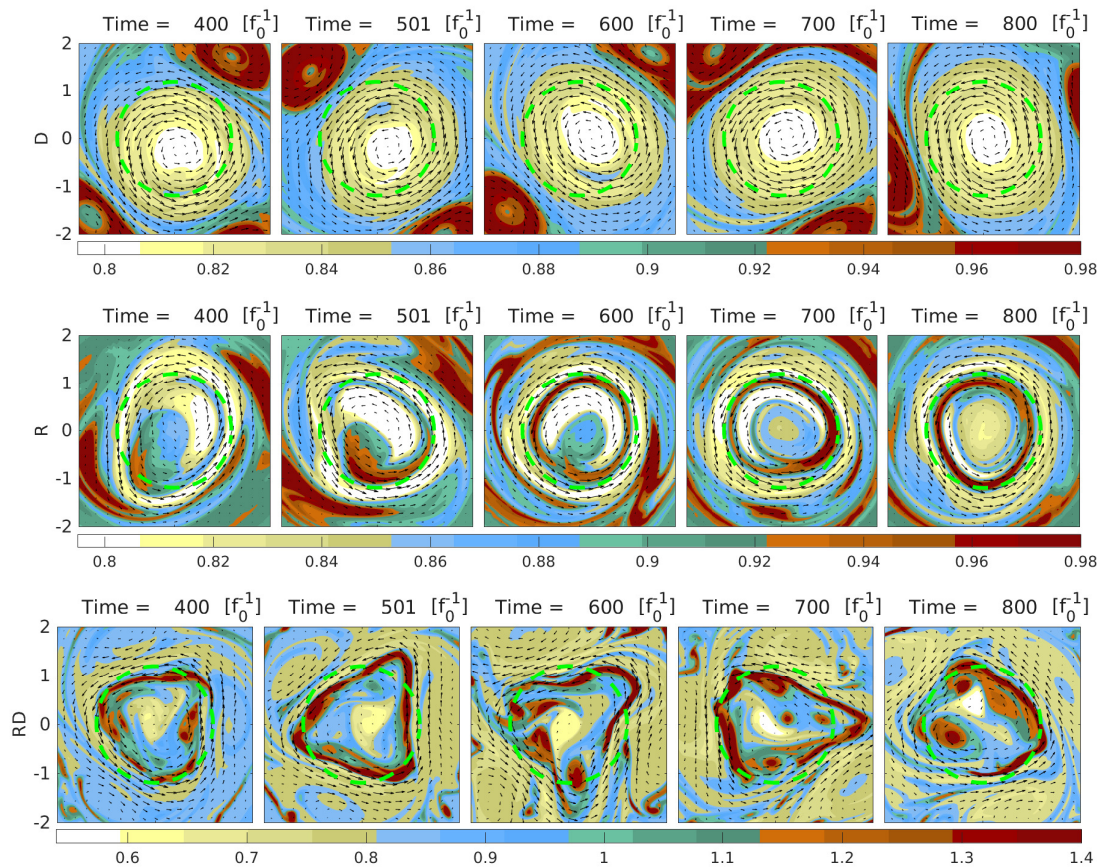
33

Figure 12. Same as figure 11 for later times.

that it is based on momentum and mass conservation with only a couple of ba-sic parametrisations. It is thus robust and does not rely on numerous fine-tuned parametrisations of physical processes. The model captures only the most basic features of the dynamics, which however turns to be sufficient to understand the salient properties of the Mars' polar vortex. The model can be improved in many ways by including topographic effects, nuclei (dust) sources and sinks, but also by passing from its barotropic version to a two- or multi-layer baroclinic version, which would allow to include the effects of stratification and wind shear.

We should emphasize that in the present study we were attempting to gain a gen-

eral understanding of the respective roles of deposition and radiative relaxation, without making an effort to adjust parameters and initializations to fit the observations in the best possible way. Nevertheless, we sketched general dependencies of the results on the values of the parameters. Neither we introduce topography which, as already mentioned in Introduction, could account for the ellipticity of the polar vortex. Data assimilation techniques can be straightforwardly applied to the model with realistic topography, if necessary, but this was not our goal here.

Acknowledgements

References

Barnes, J. R., 1984. Linear baroclinic instability in the martian atmosphere. Journal of the Atmospheric Sciences 41 (9), 1536–1550.

Barnes, J. R., Haberle, R. M., Pollack, J. B., Lee, H., Schaeffer, J., 1996. Mars atmospheric dynamics as simulated by the nasa ames general circulation model: 3. winter quasi-stationary eddies. Journal of Geophysical Research: Planets 101 (E5), 12753–12776.

Barnes, J. R., Pollack, J. B., Haberle, R. M., Leovy, C. B., Zurek, R. W., Lee, H., Schaeffer, J., 1993. Mars atmospheric dynamics as simulated by the nasa ames general circulation model: 2. transient baroclinic eddies. Journal of Geophysical Research: Planets 98 (E2), 3125–3148.

Bouchut, F., Lambaerts, J., Lapeyre, G., Zeitlin, V., 2009. Fronts and nonlinear waves in a simplified shallow-water model of the atmosphere with moisture and convection. Physics of Fluids 21 (11).

Colaprete, A., Toon, O. B., 2003. Carbon dioxide clouds in an early dense martian atmosphere. Journal of Geophysical Research: Planets 108 (E4), 5025.

Conrath, B. J., Nov. 1981. Planetary-scale wave structure in the martian atmosphere. Icarus 48, 246–255.

Eckermann, S. D., Ma, J., Zhu, X., 2011. Scale-dependent infrared radiative damping rates on mars and their role in the deposition of gravity-wave momentum flux. Icarus 211 (1), 429 – 442.

González-Galindo, F., Forget, F., López-Valverde, M. A., Angelats i Coll, M., Millour, E., 2009. A ground-to-exosphere martian general circulation model: 1. seasonal, diurnal, and solar cycle variation of thermospheric temperatures.

Journal of Geophysical Research: Planets 114 (E4), n/a–n/a, e04001.

González-Galindo, F., Määttänen, A., Forget, F., Spiga, A., 2011. The martian mesosphere as revealed by co2 cloud observations and general circulation modeling. Icarus 216 (1), 10–22, cited By :20.

Goody, R., Belton, M. J., 1967. A discussion of martian atmospheric dynamics. Planetary and Space Science 15 (2), 247 – 256.

Greybush, S. J., Wilson, R. J., Hoffman, R. N., Hoffman, M. J., Miyoshi, T., Ide, K., McConnochie, T., Kalnay, E., 2012. Ensemble kalman filter data assimilation of thermal emission spectrometer temperature retrievals into a mars gcm. Journal of Geophysical Research: Planets 117 (E11), e11008.

Hartmann, D. L., 1983. Barotropic instability of the polar night jet stream. Journal of the Atmospheric Sciences 40 (4), 817–835.

Hayne, P. O., Paige, D. A., Schofield, J. T., Kass, D. M., Kleinböhl, A., Heavens, N. G., McCleese, D. J., 2012. Carbon dioxide snow clouds on mars: South polar winter observations by the mars climate sounder. Journal of Geophysical Research: Planets 117 (E8), e08014.

Hollingsworth, J. L., Barnes, J. R., 1996. Forced stationary planetary waves in mars's winter atmosphere. Journal of the Atmospheric Sciences 53 (3), 428–448.

Hoskins, B. J., Bretherton, F. P., 1972. Atmospheric frontogenesis models: Mathematical formulation and solution. Journal of the Atmospheric Sciences 29 (1), 11–37.

Hu, R., Cahoy, K., Zuber, M. T., 2012. Mars atmospheric co2 condensation above the north and south poles as revealed by radio occultation, climate sounder, and laser ranging observations. Journal of Geophysical Research: Planets 117 (E7),

e07002.

Imamura, T., Ogawa, T., 1995. Radiative damping of gravity waves in the terrestrial planetary atmospheres. Geophysical Research Letters 22 (3), 267–270.

Lewis, S. R., 2003. Modelling the martian atmosphere. Astronomy and Geophysics 44 (4), 4.06–4.14.

Listowski, C., Määttänen, A., Montmessin, F., Spiga, A., Lefèvre, F., 2014. Modeling the microphysics of co2 ice clouds within wave-induced cold pockets in the martian mesosphere. Icarus 237, 239–261, cited By :8.

López-Puertas, M., López-Valverde, M., 1995. Radiative energy balance of co2 non-lte infrared emissions in the martian atmosphere. Icarus 114 (1), 113 – 129.

López-Valverde, M. A., Edwards, D. P., López-Puertas, M., Roldán, C., 1998. Non-local thermodynamic equilibrium in general circulation models of the martian atmosphere 1. effects of the local thermodynamic equilibrium approximation on thermal cooling and solar heating. Journal of Geophysical Research: Planets 103 (E7), 16799–16811.

Määttänen, A., Vehkamäki, H., Lauri, A., Merikallio, S., Kauhanen, J., Savijärvi, H., Kulmala, M., Feb. 2005. Nucleation studies in the Martian atmosphere. Journal of Geophysical Research (Planets) 110, E02002.

Mahaffy, P. R., Webster, C. R., Atreya, S. K., Franz, H., Wong, M., Conrad, P. G., Harpold, D., Jones, J. J., Leshin, L. A., Manning, H., Owen, T., Pepin, R. O., Squyres, S., Trainer, M., , 2013. Abundance and isotopic composition of gases in the martian atmosphere from the curiosity rover. Science 341 (6143), 263–266.

Michelangeli, D. V., Zurek, R. W., Elson, L. S., 1987. Barotropic instability of midlatitude zonal jets on mars, earth and venus. Journal of the Atmospheric

Sciences 44 (15), 2031–2041.

Mitchell, D. M., Montabone, L., Thomson, S., Read, P. L., 2015. Polar vortices on Earth and Mars: A comparative study of the climatology and variability from reanalyses. Quarterly Journal of the Royal Meteorological Society 141 (687), 550–562.

Montabone, L., Marsh, K., Lewis, S. R., Read, P. L., Smith, M. D., Holmes, J., Spiga, A., Lowe, D., Pamment, A., 2014. The mars analysis correction data assimilation (MACDA) dataset v1.0. Geoscience Data Journal 1 (2), 129–139.

Pettengill, G. H., Ford, P. G., 2000. Winter clouds over the north martian polar cap. Geophysical Research Letters 27 (5), 609–612.

Rong, P., Waugh, D. W., 2004. Vacillations in a shallow-water model of the stratosphere. Journal of the Atmospheric Sciences 61 (10), 1174–1185.

Rostami, M., Zeitlin, V., 2017. Influence of condensation and latent heat release upon barotropic and baroclinic instabilities of vortices in a rotating shallow water f-plane model. Geophysical & Astrophysical Fluid Dynamics 111 (1), 1–31.

Rostami, M., Zeitlin, V., 2018. Improved moist-convective rotating shallow water model and its application to instabilities of hurricane-like vortices. Quarterly Journal of the Royal Meteorological Society.

Rostami, M., Zeitlin, V., Spiga, A., 2017. On the dynamical nature of saturn's north polar hexagon. Icarus 297, 59 – 70.

Seviour, W. J. M., Scott, R. K., Waugh, D. W., 2017. The stability of mars' annular polar vortex. Journal of the Atmospheric Sciences.

Toigo, A. D., Waugh, D. W., Guzewich, S. D., 2017. What causes mars' annular

polar vortices? Geophysical Research Letters 44 (1), 71–78, 2016GL071857.

Trefethen, L., 2000. Spectral Methods in MATLAB. Society for Industrial and Applied Mathematics.

Waugh, D. W., Toigo, A. D., Guzewich, S. D., Greybush, S. J., Wilson, R. J., Montabone, L., 2016. Martian polar vortices: Comparison of reanalyses. Journal of Geophysical Research: Planets 121 (9), 1770–1785, 2016JE005093.

Wood, S. E., 1999. Nucleation and growth of co_2 ice crystals in the martian atmosphere. Ph.D. theis, Univ. of Calif., Los Angeles.

Zeitlin, V., 2007. Chapter 1 introduction: Fundamentals of rotating shallow water model in the geophysical fluid dynamics perspective. In: Zeitlin, V. (Ed.), Nonlinear Dynamics of Rotating Shallow Water: Methods and Advances. Vol. 2 of Edited Series on Advances in Nonlinear Science and Complexity. Elsevier Science, pp. 1 – 45.